ADVANCED NANOBIOMED RESEARCH Open Access
www.advnanobiomedres.com

A Lightweight Skin-Adhesive Fiber Bragg Grating Sensor to Advance Minimally Invasive Healthcare Monitoring

Ilaria Condò, Marcella Trombetta, Emiliano Schena, Daniela Lo Presti, and Sara Maria Giannitelli**

Wearable sensors that combine high precision with conformability and skin adhesion are crucial for reliable and highly unobtrusive physiological monitoring. In this context, increasing efforts are directed toward next-generation miniaturized self-adhesive sensors employing different sensing technologies. Herein, for the first time a self-adhesive sensor is developed for real-time detection of physiological and biomechanical strain signals, by embedding a fiber Bragg grating (FBG) sensor into a soft, biomimetic, flexible matrix. This hydrogel-based matrix, composed of gelatin methacrylate, xanthan gum, and glycerol, is engineered to balance fiber–matrix mechanical coupling and skin adhesion. The encapsulated FBG sensor exhibits stable optical response, reduced signal attenuation, and retains good sensitivity to both strain (0.07 nm mε^{-1}) and temperature (0.01 nm °C^{-1}). Preliminary on-skin tests on a healthy volunteer demonstrate the ability to capture subtle physiological signals such as breathing and heartbeats, as well as limb motion. Notably, the self-adhesive properties of the matrix enable firm skin contact without additional tapes, enhancing signal reliability, and reducing motion artifacts. This approach offers a robust, biocompatible, and scalable solution for wearable sensing, opening new opportunities in health monitoring, rehabilitation, and human–machine interfaces.

1. Introduction

Wearable technologies have rapidly evolved into key tools for personalized healthcare, enabling continuous, noninvasive monitoring of physiological signals in real-world scenarios.[1] Designed to be flexible, skin-conformal, and user-friendly, these systems aim to collect clinically relevant data without interfering with daily activities or natural body movement.[2,3] As a result, a wide range of wearable sensing devices has been developed to perform sophisticated physical and chemical monitoring of key physiological parameters such as temperature (T), cardiac and/or respiratory activity, blood pressure, joint motion, and blood glucose levels.[4–6] Considerable progress has been made in the intelligent adaptation of traditional sensing technologies—including mechanical, electrical, and optical methods—for human health monitoring applications.[7] Despite these advancements, conventional wearable sensors suffer from several limitations, including low sensitivity, hysteresis, signal drift, susceptibility to electromagnetic interference, and sensitivity to misalignment.[8] These drawbacks become even more critical in electromedical scenarios, such as during robotic actuation or magnetic resonance imaging procedures.[9] In this context, fiber-optic sensors (FOS) have emerged as a highly promising technology thanks to their transparency, small size, flexibility, low weight, biocompatibility, and immunity to electromagnetic interference.[10,11] Recently, different optical fiber configurations, such as fiber Bragg gratings (FBGs) and WaveFlex sensors, have further advanced biomedical monitoring, both in wearable sensing and biosensing applications.[10,12,13] In particular, the inherent high sensitivity of FBGs to ε and T variations (ΔT), combined with their multiplexing capabilities and chemical stability, makes them ideal for integration into next-generation wearable systems. FBG-based platforms have been successfully applied in the monitoring of cardio-respiratory activity, joint motion, and other clinically relevant parameters, including in cases where conventional electrical

---

I. Condò, E. Schena, D. Lo Presti
Measurements and Biomedical Instrumentation Research Unit
Department of Engineering
Università Campus Bio-Medico di Roma
Via Álvaro del Portillo 21, 00128 Rome, Italy
E-mail: d.lopresti@unicampus.it

The ORCID identification number(s) for the author(s) of this article can be found under https://doi.org/10.1002/anbr.202500213.

DOI: 10.1002/anbr.202500213

M. Trombetta, S. M. Giannitelli
Advanced Technologies for Innovative Materials and Organ Models Research Unit
Department of Science and Technology for Sustainable Development and One Health
Università Campus Bio-Medico di Roma
Via Álvaro del Portillo 21, 00128 Rome, Italy
E-mail: s.giannitelli@unicampus.it

E. Schena, D. Lo Presti
Fondazione Policlinico Universitario Campus Bio-Medico
Via Álvaro del Portillo 200, 00128 Rome, Italy

sensors are unsuitable due to interference or signal instability. To maximize their compatibility with the human body, FBGs have increasingly been embedded into flexible polymeric matrices.[14,15] This approach enables better ε transfer from the body to the fiber and opens the door to the integration of new functional properties, such as conformal adhesion to skin. Indeed, because most of these systems do not inherently adhere to the skin, external supports such as straps or medical adhesive tapes are typically needed to secure them, often influencing the measurement process.[14–16] In addition, the prolonged use of traditional adhesive tapes may raise biocompatibility concerns.[17] Recently, an adhesive polymeric matrix based on modified polydimethylsiloxane (PDMS) has been used to embed an FBG for the monitoring of heart rate and respiratory rate, further highlighting the potential of adhesive substrates for wearable optical sensing.[18,19] Among the available materials, hydrogels stand out due to their 3D network structure and high-water content, which endow them with excellent softness, biocompatibility, tunable mechanical properties, and tissue-mimicking behavior.[20] In recent years, adhesive hydrogels have gained growing interest in numerous technological domains, ranging from tissue repair and soft robotics to strain and biochemical sensors for healthcare applications.[21] Hence, self-adhesive hydrogel-based wearable sensors composed of soft electronics or conductive polymers have been developed to address the limitations of traditional systems, eliminating the need for external tapes or mechanical supports while improving both comfort and sensing performance.[6,7,22]

Consistently with this research direction, recent efforts has focused on embedding FBGs into functional hydrogel matrices that not only provide mechanical support but also enhance adhesion and proper ε transduction, enabling plant wearable sensors for growth monitoring.[23] This strategy appears particularly promising for on-skin health monitoring, since adhesive hydrogels, mimicking the mechanics of biological tissues and ensuring direct, conformal skin contact, could thereby enable intimate mechanical coupling and more efficient strain transfer.

With the aim of translating this technology to biomedical applications, biocompatible materials were taken into consideration to develop a skin-adhesive and skin-safe hydrogel matrix for FBG encapsulation and prolonged contact with human skin.[24,25] Among these, gelatin methacrylate (gelMA) has been extensively studied for its use in biomedical hydrogels due to its structural tunability, its ability to be photocrosslinked, and capacity to mimic human tissues.[24,26,27] In parallel, xanthan gum (XG)—a natural and edible polysaccharide—is being increasingly used to enhance the mechanical robustness and rheological properties of hydrogel systems.[28–30] Moreover, glycerol—a nonvolatile, colorless and hygroscopic liquid—was incorporated as a plasticizer, since it is widely used to enhance flexibility and water retention in polymeric systems.[31,32] Overall, the synergistic interplay among these components is expected to yield a soft, self-adherent matrix, well-suited for direct skin application without external supports.

Here, we present a flexible wearable sensor based on an FBG encapsulated within a self-adhesive hydrogel-based matrix (which we referred to as gelMA-XG), specifically designed for on-skin wearable physiological signals monitoring via strain sensing. The matrix was easily prepared using a one-pot strategy combining gelMA, XG and glycerol, all of which are well-established as biocompatible for extended skin-contact applications.[29,30,33,34] The key innovation of this work lies in the first demonstration, at date, of an FBG sensor fully integrated within a soft, skin-conformable adhesive hydrogel-based matrix. This design ensures both firm epidermal adhesion and intimate mechanical coupling with the optical fiber, resulting in a tape-free FBG-based wearable sensor. This configuration enables the sensor to function as a single body-sensor unit, capable of detecting both macro- and microscopic skin deformations with high fidelity. To realize this, the workflow was structured into three main phases: 1) formulation and characterization of candidate hydrogels to identify the optimal matrix; 2) fabrication and metrological characterization of the flexible sensor to evaluate how the matrix affects the intrinsic performance of the enclosed FBG; 3) preliminary on-skin feasibility tests on a healthy volunteer to validate the sensor ability to operate in real-world physiological scenarios. This work introduces a new class of self-adhesive optical-based epidermal sensors and lays the groundwork for future advancements in minimally invasive and high-performance wearable technologies.

2. Optical Fibers and Working Principle of FBGs

Optical fibers are cylindrical, flexible, transparent waveguides made of plastic or silica, composed of three concentric layers: a central core, a surrounding cladding with a lower refractive index, and an outer protective coating. Light is guided along the core by total internal reflection at the core–cladding interface. Standard single-mode fibers, commonly designed to operate in the short infrared region, generally present a core diameter of 8–10 μm and an overall diameter of about 250 μm, comparable to a human hair.[35] These fibers are particularly suited for several applications due to their low signal dispersion, high sensitivity, and compatibility with fiber-optic structures such as Bragg gratings.

An FBG corresponds to a periodic modulation of the refractive index within the core of a single-mode fiber, typically operating in the short infrared region. This periodic structure, whose length is variable (i.e., ranging from 1 to 30 mm), enables the selective reflection of specific wavelengths from a broadband light source, while allowing all other wavelengths to pass through according to the Bragg condition, defined by Equation (1)

$$\lambda_B = 2\, n_{\text{eff}} \Lambda \tag{1}$$

where λ_B is the Bragg wavelength (i.e., the central wavelength of the reflected spectrum), n_{eff} is the effective refractive index of the fiber core, and Λ is the grating period.

FBGs are inherently sensitive to mechanical ε and ΔT, both of which induce changes in n_{eff} and Λ, resulting in a shift from the initial λ_B ($\Delta\lambda_B$) which is described by Equation (2)

$$\Delta\lambda_B = (1 - p_e)\, \lambda_B\, \Delta\varepsilon + (\alpha + \eta)\, \lambda_B\, \Delta T \tag{2}$$

In this expression, p_e denotes the photoelastic coefficient related to the $\Delta\varepsilon$ contribution to $\Delta\lambda_B$, whereas α and η correspond to the thermal expansion and thermo-optic coefficients of the fiber, respectively.[36] The trend of $\Delta\lambda_B$ in time usually represents the output signal of an FBG. For a bare FBG (i.e., an FBG without any external coating material or structure), typical sensitivity values are $\approx$1.2 nm mε^{-1} for ε (S_ε) and $\approx$0.01 nm °C^{-1} for T (S_T).[37]

However, when the optical fiber is embedded within an external substrate, these sensitivities may deviate from their nominal values, as they are influenced by the thermal and mechanical properties of the surrounding material. Hence, the response of an FBG in embedded configurations is expected to differ from the bare one.

3. Results and Discussion

3.1. Design and Development of the Self-Adhesive Matrix

The proposed wearable sensor was developed by embedding an FBG within a novel self-adhesive hydrogel-based matrix composed of gelMA, XG, and glycerol. To identify the gelMA-XG matrix with the optimal adhesion to both the fiber and the skin, three formulations were investigated, differing only in the glycerol content. 10%, 15%, and 20% glycerol mass percentages were selected in this work. Glycerol was selected as the only variable due to its known role as a plasticizing and water-retaining agent that influences the mechanical behavior of hydrogel-based systems.[31,38] The detailed composition of each formulation is summarized in **Table 1**.

The hydrogel mixtures were successfully prepared through a stepwise one-pot strategy at controlled T, under continuous magnetic stirring for about 3 h (**Figure 1**). GelMA, previously synthesized, was first dissolved in deionized water (DIW) at 45 °C. Once homogeneous, T was set at 37 °C and glycerol was added to the solution, followed by the photoinitiator (LAP), that enables UV-induced crosslinking of the gelMA methacrylate groups, and by the XG, incorporated to increase the viscosity and impart a rubber-like consistency to the mixture.[25] The solution was then degassed to remove air bubbles, cast into a custom mold and irradiated with UV light (i.e., 365 nm for 5 min) to promote photocrosslinking. Finally, the cured hydrogels were removed from the mold and dried in a laboratory oven at 37 °C for 24 h, leading to flexible adhesive films. Further technical information regarding the matrix fabrication process is detailed in the Experimental Section.

Table 1. Composition of gelMA-XG matrices. Glycerol content ($\%_{w/w}$) is indicated as subscript in the gelMA-XG label.

label	Glycerol [%]	Glycerol [g]	GelMA [g]	XG [g]	LAP [g]	DIW [g]
gelMA-XG$_{10}$	10	1	0.25	0.1	0.025	8.625
gelMA-XG$_{15}$	15	1.5	0.25	0.1	0.025	8.125
gelMA-XG$_{20}$	20	2	0.25	0.1	0.025	7.625

The formation of a covalent polymeric network via UV-induced photopolymerization of gelMA provided the material with structural mechanical integrity. Moreover, the slow drying step, which enables the controlled removal of excess water, contributes to the long-term stability of the hydrogel matrix.[30]

To assess how the glycerol content affects the mechanical properties of the hydrogel matrix, a uniaxial tensile test was conducted on the three formulations. Samples were prepared by casting the mixtures into dog-bone shaped molds and then tested at room temperature (RT). **Figure 2**A displays representative stress–strain curves for each formulation.

The Young's modulus (i.e., 42.5 ± 4.5, 20.4 ± 3.2, and 10.6 ± 1.8 kPa for gelMA-XG$_{10}$, gelMA-XG$_{15}$, and gelMA-XG$_{20}$, respectively), along with the maximum tensile strength and the elongation at break, decreased with increasing glycerol content, in agreement with literature evidence on the plasticizing character of the glycerol (Figure 2B–D).[31] Indeed, its ability to retain water molecules decreases intermolecular forces within the hydrogel, reducing the rigidity of the hydrogel network, and making the gelMA-XG$_{20}$ more elastic and at the same time less resistant to traction.

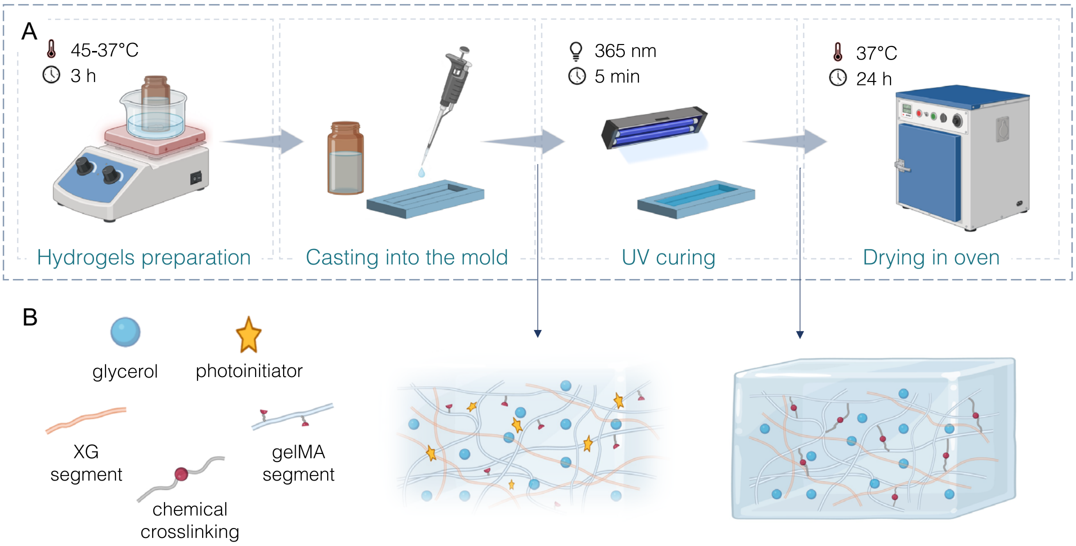

Figure 1. A) Workflow for the preparation of gelMA-XG matrices: dissolution of the components in DIW under heated magnetic stirring, casting of the obtained hydrogel solution into a custom mold, UV-induced crosslinking, and drying of the matrices in a laboratory oven. B) Schematic representation of the microstructure of a gelMA-XG matrix before (left) and after (right) UV curing, highlighting the formation of chemical crosslinks between the methacrylated groups of gelMA. Partially created with BioRender.com.

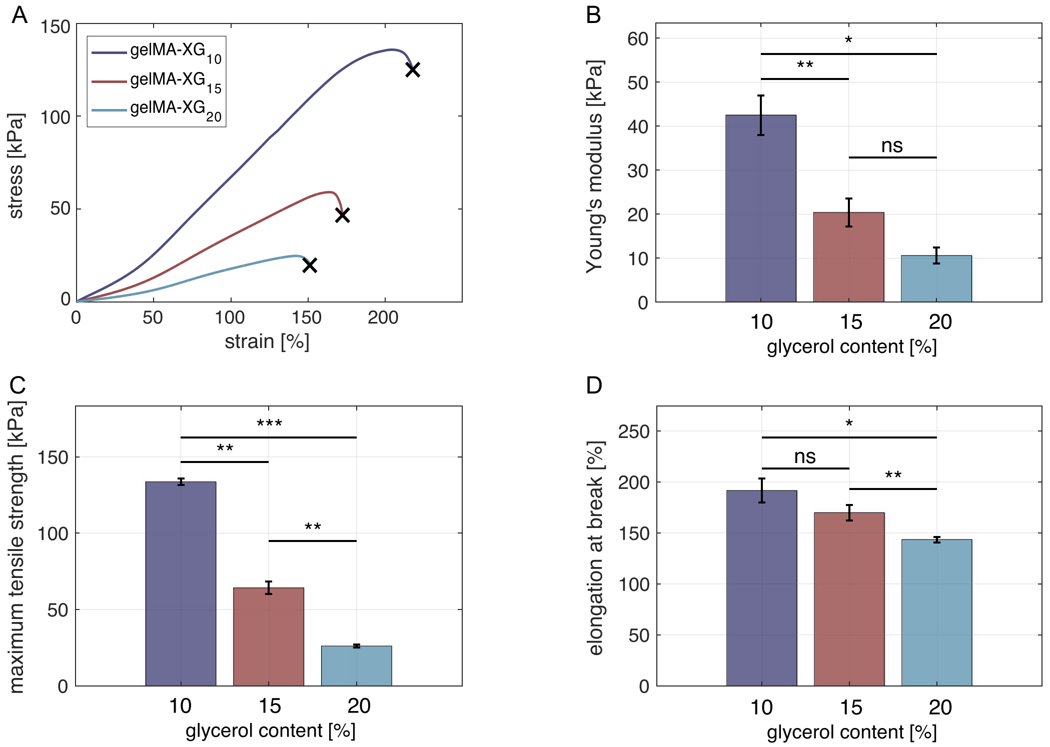

Figure 2. Mechanical characterization of gelMA-XG hydrogel matrices. A) Representative tensile stress–strain curves of the three matrices, gelMA-XG$_{10}$, gelMA-XG$_{15}$ and gelMA-XG$_{20}$. B) Young's modulus, C) maximum tensile strength, and D) elongation at break as a function of glycerol content. Data are reported as mean ± standard deviation (SD) ($n = 3$). Pairwise two-sided t-test were performed. Significance: $p < 0.05$ (*), $p < 0.01$ (**), $p < 0.001$ (***), ns = not significant.

Moreover, the dimensional stability of the hydrogel matrices during the drying phase was evaluated by measuring the thickness of each sample before and after the 24 h-incubation at 37 °C. By comparing obtained thickness reduction values ($\Delta\delta$), gelMA-XG$_{10}$ exhibited the greatest $\Delta\delta$ ($80 \pm 2\%$), while the gelMA-XG$_{15}$ and gelMA-XG$_{20}$ showed progressively lower shrinkage ($71 \pm 2\%$ and $72 \pm 1\%$, respectively). This trend is consistent with the mechanical observations, where increased glycerol content softened the network, but also limited collapse upon drying, likely due to the hygroscopic nature of glycerol.

The interfacial adhesion properties of the hydrogel matrices were evaluated through pull-out and lap shear tests to investigate two distinct types of interaction. The pull-out test was conducted to quantify the internal shear strength at the fiber–hydrogel interface, whereas the lap shear test assessed the adhesiveness of the hydrogel matrix to external substrates.

For the pull-out test, a custom 3D-printed support was designed to minimize matrix deformation and test artifacts due to material elasticity. As shown in **Figure** 3A, the sample was clamped between two glass coverslips to constrain deformation and isolate interfacial shear strength at the fiber–hydrogel boundary. Among the tested formulations, gelMA-XG$_{10}$ exhibited the highest τ_{app} (i.e., 157.7 ± 11.8 kPa), approximately three times higher than that of gelMA-XG$_{20}$, while gelMA-XG$_{15}$ presented an intermediate value (Figure 3B). These results can be attributed to the reduced mechanical integrity and cohesive strength of gelMA-XG$_{20}$, whose higher glycerol content weakens the matrix ability to resist fiber detachment. A stronger fiber–matrix interaction is crucial for an efficient ε transmission to the embedded FBG sensor, ultimately improving the reliability and sensitivity of the sensing system.

The adhesive behavior of the gelMA-XG matrices arises from the synergistic contribution of their components' properties. XG, in combination with glycerol, imparts viscoelasticity and softness, enabling the matrix to closely conform to the irregularities of the skin and thereby increase the effective contact area. In parallel, the abundance of polar functional groups (e.g., –NH, –OH, –COOH) in gelMA, XG, and glycerol promotes hydrogen bonding and polar interactions with epidermal proteins and lipids. Glycerol, acting as a hygroscopic plasticizer, preserves hydration and flexibility of the matrix, stabilizing the interface. The combination of these effects results in reversible adhesion, consistently with previous reports on similar hydrogel-based matrices.[30] Adhesion was quantitatively assessed through the lap shear test, conducted by placing hydrogel films between two pigskin substrates, selected as a biologically relevant model of human skin (Figure 3C).[39] In contrast to the pull-out results, gelMA-XG$_{20}$ showed the highest adhesive strength (4.34 ± 0.41 kPa), followed by gelMA-XG$_{15}$ and then gelMA-XG$_{10}$ (Figure 3D). This reverse trend can be easily attributed to the enhanced compliance of the matrices when glycerol content increases. Two main mechanisms are responsible for this improved adhesion: 1) the presence of a greater number of polar functional groups that enhances intermolecular interactions with the substrate and

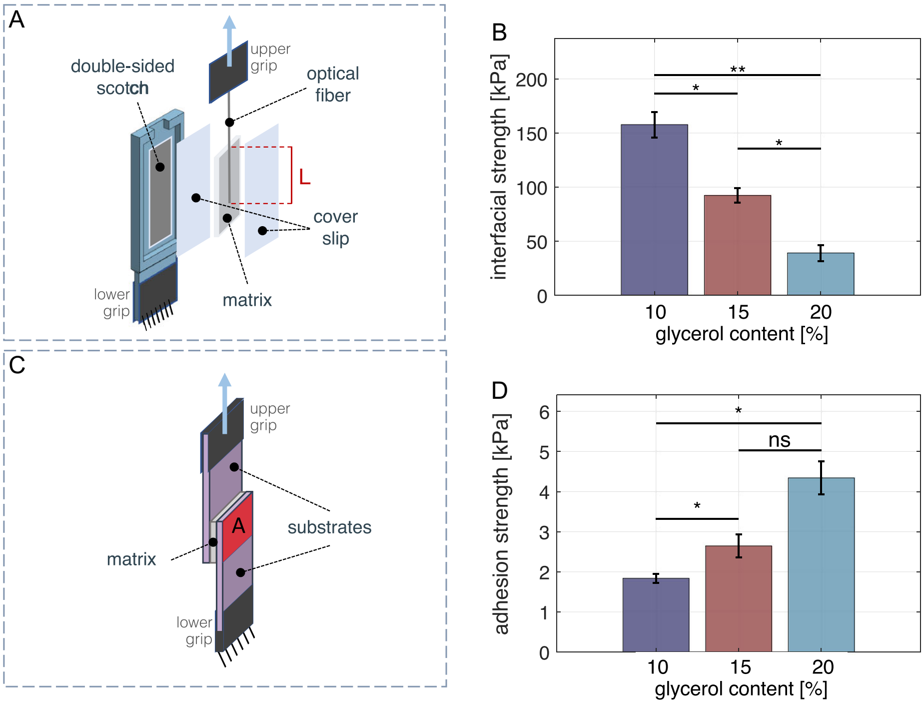

Figure 3. Interfacial adhesion properties of gelMA-XG matrices. A) Schematic diagram of the experimental setup for the customized pull-out test (L: length of the section where fiber and material interface). B) Bar chart highlighting the effect of glycerol content on the apparent interfacial shear strength. C) Schematic experimental setup for the lap shear test (A: adhesive area between the matrix and the two pigskin substrates). D) Bar chart highlighting the effect of glycerol content on the adhesion strength. Data are reported as mean ± standard deviation (SD) ($n = 3$). Pairwise two-sided *t*-test were performed. Significance: $p < 0.05$ (*), $p < 0.01$ (**), $p < 0.001$ (***), ns = not significant.

2) the increased softness of the matrix that allows for a larger effective contact area and promotes better mechanical interlocking with the microroughness of the skin surface.[30,38]

Taken together, these findings reveal a trade-off between internal fiber–matrix integration and external skin adhesiveness: lower glycerol concentrations enhance mechanical cohesion and fiber retention, while higher concentrations favor adhesion to soft biological tissues through improved conformability and interfacial interactions.

Given that the hydrogel is intended to host an embedded optical fiber—which inherently limits the overall extensibility of the system—high stretchability is not a primary requirement. Instead, the matrix must provide adequate mechanical support to protect the fiber and ensure good ε transmission, while also maintaining good adhesion to the skin to preserve conformal contact during body movements.

In light of these considerations, gelMA-XG$_{15}$ was identified as the optimal compromise for the intended application. This formulation offers a balanced combination of mechanical robustness, reduced shrinkage, effective fiber integration, and sufficient skin adhesion, making it the most suitable candidate for the development of the FBG-based skin-adhesive sensor.

Once gelMA-XG$_{15}$ was established as the most suitable formulation, its adhesive performance was further investigated in terms of interaction with human skin, reusability, and adhesion to different substrates. A rectangular sample of the selected material was applied to the forearm of a healthy subject to qualitatively evaluate epidermal conformability, adhesion, and removability. The matrix adhered closely and uniformly to the skin, maintaining contact even during natural movements of the arm, with no evidence of slippage or delamination. Upon removal, the matrix sample detached cleanly without leaving visible residues, supporting its suitability for tape-free and comfortable on-skin application (**Figure** 4A).

To quantify the adhesive force required to peel the material from human skin and to evaluate its potential reusability, a controlled 90° peel test was performed (see Figure 4B). The same rectangular matrix (70 × 15 mm) was repeatedly applied to the forearm skin and peeled off for 30 consecutive times, while recording the adhesion force in each cycle. The number of 30 repetitions was chosen to simulate the adhesion performance of a wearable device over approximately one month of use. Figure 4C shows that during the first 20 cycles the adhesive force remained stable around 0.124 ± 0.007 N, demonstrating optimal adhesion and reliable reusability over 20 uses (i.e., attach–detach). In the subsequent ten cycles, a slight reduction in the peel force was observed, with values going below the average estimated over the overall cycles (i.e., a mean value decrease of ≈8.4%). Nevertheless, the matrix maintained adequate adhesive capacity throughout, demonstrating its suitability for repeated applications on skin as a component of a wearable system.

Finally, qualitative adhesion tests were conducted on various representative substrates, including aluminum foil, glass, paper, plastic, wood, and cork, to further assess its practical adhesive properties. As shown in Figure 4D, the gelMA-XG$_{15}$ hydrogel adhered effectively to all surfaces without the need for surface

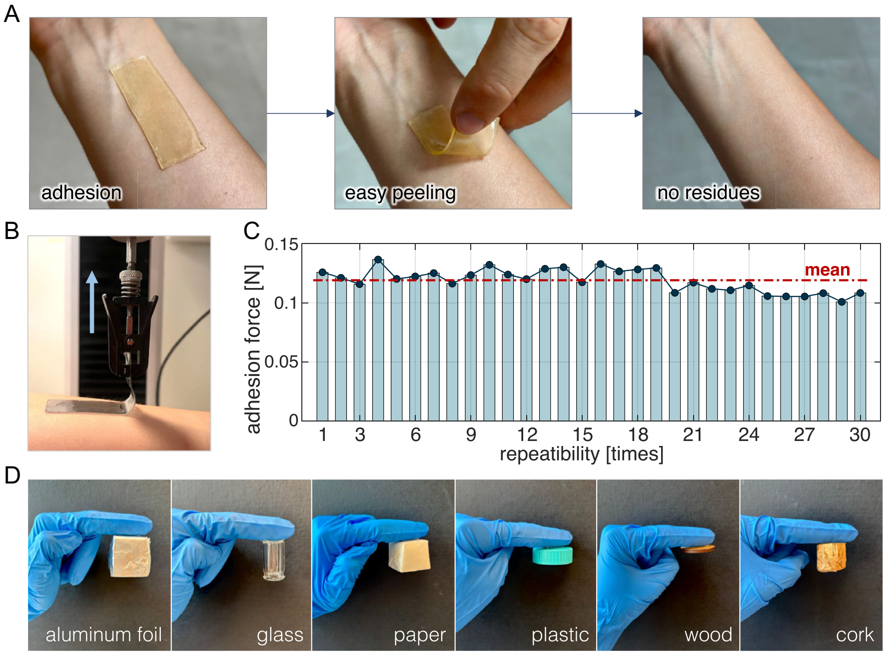

Figure 4. Adhesion properties of the gelMA-XG$_{15}$ matrix. A) Exhibition of the matrix peeling process on a human forearm skin; no residues visibly remain on the skin after removal. B) A rectangular sample gripped to a universal testing machine for peel testing and C) adhesion force values recorded over 30 consecutive tests on a human forearm; the mean adhesion force over the 30 attach–detach cycles is reported as a red dashed line. D) Demonstration of the matrix adhesiveness on different surfaces, including aluminum foil, glass, paper, plastic, wood, and cork (targets weight ranging from 3 to 5 g). For aluminum foil and paper, coated polystyrene cubes were used to facilitate the visibility of the targets.

pretreatment or curing agents, confirming a broad interfacial compatibility.

3.2. Development of the Adhesive Wearable Sensor

The wearable sensor was successfully fabricated by encapsulating a single FBG within the gelMA-XG$_{15}$ adhesive hydrogel-based matrix having final dimensions of $50 \times 20 \times 1.5$ mm (**Figure** 5A,B). The sensing mechanism relies on the ε transmission through mechanical coupling between the human skin and the matrix, which is then transduced by the embedded FBG. Due to the novelty of the matrix, a proper metrological characterization was conducted to evaluate its potential impact on the FBG sensing properties prior to any feasibility assessment on a healthy human volunteer.

The FBG reflected spectrum was recorded before and after the hydrogel drying process. As shown in Figure 5C, no significant variation was observed in terms of spectral intensity or full width at half maximum (FWHM), indicating stable grating characteristics within the matrix. However, a minor red shift in λ_B of $\approx$0.048 nm was detected postdrying, suggesting the presence of residual ε on the fiber. The temporal evolution of the $\Delta\lambda_B$, reported in Figure 5D, reveals an initial compressive phase (a blueshift of 0.035 nm) during the first 5 h, likely caused by matrix shrinkage as water begins to evaporate. This is followed by a progressive tensile phase, attributable to the final drying stage, in which the final hydrogel contraction may exert localized traction on the sensing segment of the fiber—specifically at its central region, where it is positioned—resulting in a uniaxial tensile strain on the fiber. This behavior confirms that the fiber is effectively mechanically coupled to the matrix and experiences internal stress as the material dry, further supporting the embedding strategy for wearable sensing applications.

The metrological performance of the FBG-based adhesive sensor was evaluated in terms of its sensitivity to both ε and T (i.e., the two primary measurands to which a bare FBG is inherently responsive). Calibration tests were performed on the selected gelMA-XG$_{15}$ formulation by applying controlled uniaxial mechanical ε and ΔT.

The strain calibration curve $\Delta\lambda_B$ versus ε, reported in Figure 5E, exhibited a strong linearity and was well-fitted by a first-order polynomial, whose goodness was confirmed by an $R^2 > 0.99$. S_ε, measured as the slope of the calibration curve, was found to be 0.070 nm mε^{-1}. This value is lower than the typical S_ε of a bare FBG ($\approx$1.2 nm mε^{-1}), as expected due to the viscoelastic properties of the encapsulating hydrogel, which partially attenuates the mechanical ε transmitted to the fiber. Despite this reduction, the sensor maintains a sufficiently high S_ε, making it suitable for detecting ε variations within the physiological range. Notably, similar reductions in S_ε have been reported in other polymer-embedded FBG-based sensors, confirming that this behavior is intrinsic to embedded configurations.[23,40,41]

S_T was assessed by exposing the sensor to a controlled ΔT (i.e., $\approx$30 °C) within the 20–50 °C range. The resulting S_T was measured as the slope of the calibration curve $\Delta\lambda_B$ versus ΔT, obtained by linear fitting raw data ($R^2 > 0.99$) (Figure 5F). The obtained value of 0.009 nm °C^{-1} closely matched the nominal value for a bare FBG ($\approx$0.010 nm °C^{-1}), suggesting that the

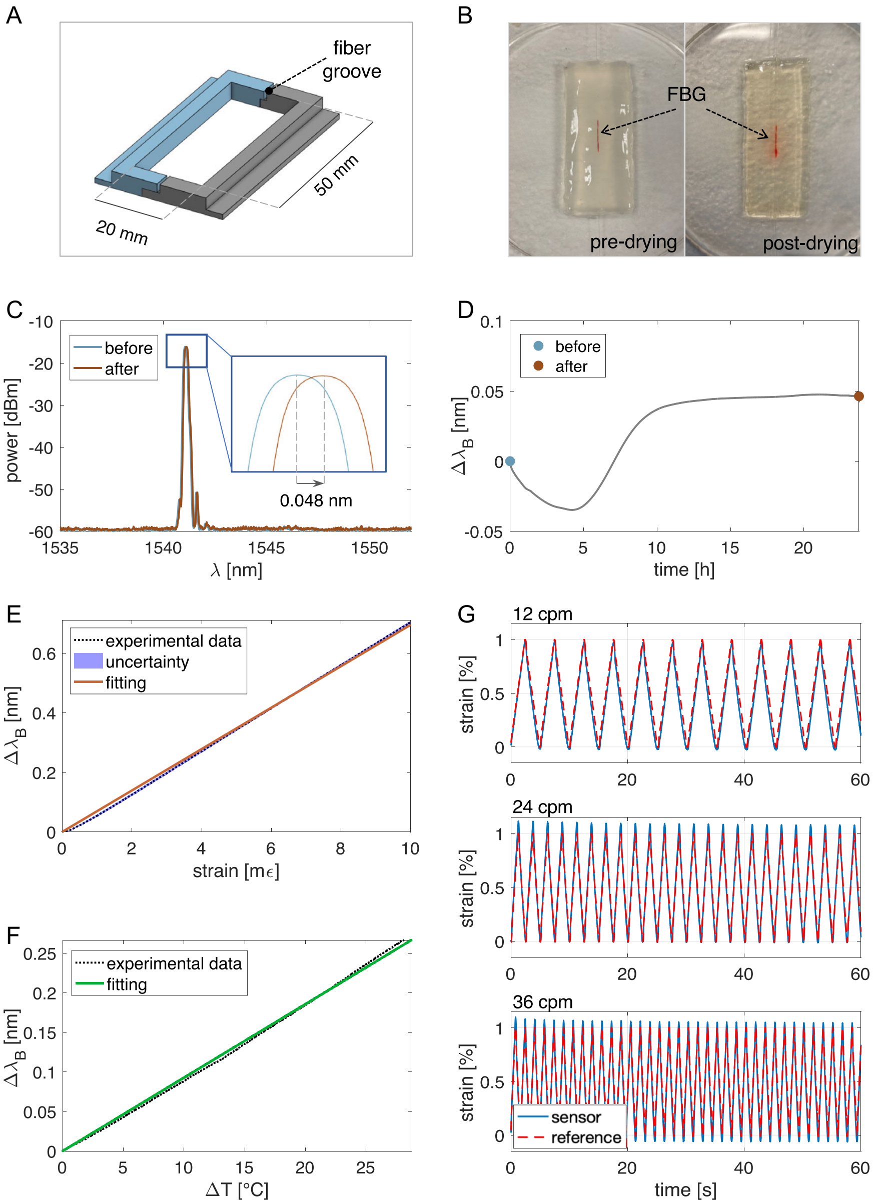

Figure 5. Development and calibration of the adhesive FGB-based sensor. A) CAD model of the PLA mold. B) The fabricated adhesive wearable sensor composed of an FBG embedded into an adhesive hydrogel-based matrix. Pictures of the sensor are reported before and after the drying stage. C) Reflection spectra of the FBG before and after the drying phase of the matrix preparation process. A zoomed-in view on the reflected peak highlights a red shift of 0.048 nm in the spectrum following this phase. D) Time response of the FBG within the matrix during the drying phase. The colored dots (i.e., blue and brown) indicate the time points at which the corresponding spectra shown in (C) were acquired. E) Mean $\Delta\lambda_B$ versus ε curve is reported in black with the expanded uncertainty in a violet shaded area and the calibration curve in red (linear fit, $R^2 > 0.99$) ($n = 10$). F) Thermal calibration curve $\Delta\lambda_B$ vs. ΔT where the response is in black and the calibration curve in green (linear fit, $R^2 > 0.99$) ($n = 1$). G) Repetitive test at three different strain rates (12, 24, and 36 cpm) showed in a 60 s time window; the FBG sensor output is represented in blue, while the reference displacement is in dashed red. Both trends were represented as ε (i.e., in the range of 0%–1%), by dividing $\Delta\lambda_B$ by the found S_ε, and displacement by the initial length (i.e., l_0), respectively.

matrix does not significantly impact the sensor thermal response under the typical operating conditions.

To further evaluate the sensor dynamic performance, cyclic tensile tests were conducted under controlled displacement at frequencies corresponding to 12, 24, and 36 cycles per minute (cpm). Figure 5G shows a representative time window of 60 s, where the three strain rates can be observed. The recorded $\Delta\lambda_B$ output signals followed the applied cycles with high accuracy, showing well-defined periodic trends.

Across all tested frequencies, the embedded FBG sensor displayed highly repeatable and stable responses, with no observable signal lag or distortion relative to the mechanical reference, guaranteeing an optimal time response to rapid periodic physiological changes. The recorded $\Delta\lambda_B$ signals showed clear periodicity, maintaining consistent amplitude and phase alignment with the applied strain cycles. This confirms that the sensor retains responsiveness and resolution even under dynamic conditions. The consistent tracking ability across increasing frequencies highlights the capability of the sensor–matrix system to operate in real-world scenarios involving rapid and repetitive motion, such as joint articulation or cardio-respiratory activity.

3.3. Sensor Feasibility Assessment

Simple preliminary trials were performed by a healthy volunteer to test the performance of FBG-based adhesive sensor in a realistic scenario. The sensor was positioned on four anatomical sites: the neck and chest for cardio-respiratory monitoring, and the wrist and knee for joint motion detection. Sensor placement on the body is illustrated in **Figure 6**A.

When applied on the neck and chest, the volunteer was asked to hold the breath for ≈20 s, followed by a phase of quiet breathing. During apnea, the $\Delta\lambda_B$ signal flattened, confirming the sensor ability to detect real-time interruptions in respiratory activity. In both sites, the sensor reliably captured respiratory acts, which were more pronounced on the chest due to the larger thoracic movements during breathing (Figure 6B). Notably, during apnea phases, a cardiac-related signal was also observed. In particular, the neck signal also exhibits high-frequency components superimposed on the breathing pattern, consistent with heartbeats of the volunteer (Figure 6C).

At level of the wrist and knee, the volunteer performed mild flexion–extension movements. The corresponding $\Delta\lambda_B$ signals reflected the joint motion cycles. As expected, the signal amplitude was significantly higher at the knee than at the wrist, due to the greater range of motion and higher mechanical ε associated with lower-limb articulation (Figure 6D,E).

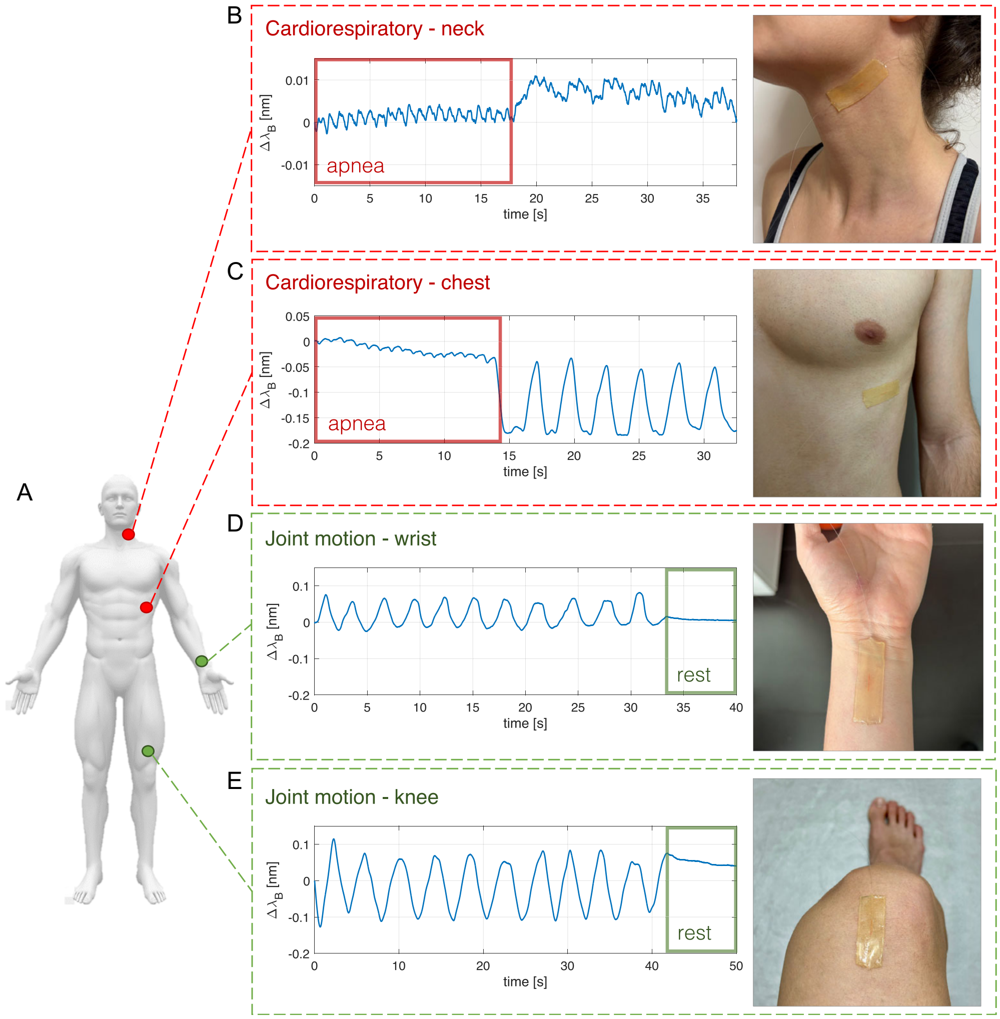

Figure 6. Detection of physiological strain signals on human skin related to cardio-respiratory activity of joint motion performing a preliminary feasibility test of the developed sensor. A) Schematic for sensor placement on the volunteer. Sensor response and images of sensor placement on the B) neck and C) chest for cardio-respiratory monitoring during quiet breathing and apnea (apnea phase is highlighted in red). Sensor response and images of sensor placement on the D) wrist and E) knee for joint motion detection during cyclic flexion and rest of the wrist and the knee (rest phase is highlighted in green); here, signals are reported with the same y-axis limits to enhance amplitude differences. Data from one volunteer ($n = 1$, proof-of-concept trial).

Overall, these findings highlighted the sensor promising capability to capture both low- and high-frequency subtle physiological signals (e.g., heartbeat, breathing) and more pronounced biomechanical movements in response to different joint kinematics (e.g., limb motion), benefiting from the high sensitivity of FOS and the enhanced mechanical coupling provided by the soft, adhesive, skin-conforming matrix.

The ability to resolve multiscale dynamic events, combined with strong skin compliance, underscores the potential of this hydrogel–FBG system as a soft wearable platform for continuous health and movement monitoring, by enhancing the intrinsic sensing performance of FBGs, through synergistic integration with the skin-compliant hydrogel matrix.

4. Conclusion

The integration of FBGs into flexible, self-adhesive platforms represents a promising strategy for developing minimally invasive wearable systems capable of accurate, continuous, and truly skin-conformal physiological monitoring. FBGs are renowned for their high-resolution sensing performance, but their application as epidermal devices has been limited by the need for external fixation. In this work, we present a lightweight, self-adhesive optical strain sensor based on a single FBG encapsulated within a soft, flexible hydrogel matrix composed of gelMA, XG, and glycerol. The matrix was engineered to provide both skin adhesion and robust mechanical integration with the fiber, enabling efficient ε transfer and eliminating the need for tapes or external supports.

Three hydrogel formulations were explored by varying the glycerol content, which acted as a plasticizer to tune matrix softness, fiber–matrix interaction, and conformal skin adhesion. Through systematic mechanical and interfacial characterization, gelMA-XG$_{15}$ was identified as the optimal compromise. In addition, the matrix demonstrated conformal and repeatable adhesion to human skin, with peel forces maintained over multiple attach–detach cycles, further supporting its suitability for reusable and tape-free wearable sensing. The resulting FBG-based sensor exhibited stable metrological performance under both thermal and mechanical loading and showed reliable real-time tracking of physiological and biomechanical signals—including respiration, heartbeat, and joint motion—during preliminary on-skin tests.

These findings highlight the potential of hydrogel-integrated FBG sensors as soft, adhesive, reusable, and versatile platforms for wearable health monitoring. Future developments may include sensor miniaturization, shape optimization, integration into multiplexed arrays, or adaptation to different anatomical sites and motion profiles. In addition, assessing the long-term usability under extended contact with the skin will be crucial for clinical and continuous monitoring applications. Overall, the proposed approach offers a solid foundation for advancing minimally invasive optical sensing technologies, enabling precise and continuous on-skin monitoring in clinical, daily-life, or sport scenarios.

5. Experimental Section

Synthesis of GelMA: The preparation of gelMA followed a previously reported method.[24,42] In brief, type A gelatin from porcine skin (Sigma-Aldrich, USA) was dissolved at $10\%_{\mathrm{w/v}}$ in phosphate buffered saline (PBS) at 50 °C. Methacrylic anhydride (MA, Sigma-Aldrich, USA) was then slowly added to the solution (0.08 mL per g of gelatin) under vigorous stirring and allowed to react for 2 h. The mixture was subsequently diluted (1:5) in warm PBS and kept under stirring for 24 h at 50 °C. For purification, the resulting gelMA solution was dialyzed against DIW at 40 °C for 7 days (MWCO: 6–8 kDa; Spectra/Por 1, SpectrumLabs, Greece). The final product was obtained by freeze-drying (LIO5P, 5PASCAL, Italy) and stored at −20 °C.

Formulation and Preparation of GelMA-XG Hydrogels: To prepare the hydrogel-based matrices, gelMA was first dissolved in DIW ($2.5\%_{\mathrm{w/w}}$) under magnetic stirring at 45 °C. Upon complete dissolution, the T was reduced to 37 °C, and three different concentrations of glycerol ($\geq$95%; Sigma-Aldrich, USA) were added to gelMA solutions, 10%, 15%, and 20% (w/w), to obtain three formulations, which will be referred to as gelMA-XG$_{10}$, gelMA-XG$_{15}$, and gelMA-XG$_{20}$, respectively.

Lithium phenyl-2,4,6-trimethylbenzoylphosphinate (LAP; Sigma-Aldrich, USA) was then added to each formulation at $0.25\%_{\mathrm{w/w}}$ as a photoinitiator to enable UV-induced crosslinking of the gelMA network. Finally, XG ($1\%_{\mathrm{w/w}}$; Sigma-Aldrich, USA) was incorporated, and the mixtures were continuously stirred at 37 °C for $\approx$3 h until complete homogenization. To remove air bubbles, the solutions were centrifuged at 2000 rpm for 5 min (Centrifuge 5702, Eppendorf, Germany) and stored at 4 °C until use.

Preparation of Adhesive Matrices: Each hydrogel formulation was preheated to 37 °C and cast into custom-designed molds using a micropipette. Then, the assembly was exposed to UV irradiation (5 W m^{-2}, ENF-26 °C/F, Spectroline, USA) at 365 nm for 5 min to activate the photoinitiator and induce gelMA crosslinking. Following UV exposure, the hydrogel samples were removed from the molds and placed into a laboratory oven (G-Therm, AG-System BASIC, Fratelli Galli, Italy) at 37 °C for 24 h to promote dehydration and improve structural stability. The dimensions of the matrices varied depending on the specific test or application, as different custom molds were used to match the experimental requirements (e.g., pull-out, lap shear, or sensor fabrication). The corresponding film dimensions are detailed in the respective section.

Custom 3D-Printed Molds: To obtain matrices with well-defined geometries, custom molds were designed using CAD software (OnShape, PTC Inc., USA) and fabricated in polylactic acid (PLA) via fused deposition modeling (FDM) 3D printing using an Ender 3 printer (Creality, China). Molds excluded a bottom surface to facilitate demolding. For fiber-integrated samples, as for the sensor, a central longitudinal groove was designed to allow precise positioning of the optical fiber at mid-thickness, ensuring axial symmetry and consistent embedding conditions across the matrix.

Characterization of Adhesive Matrices: To assess dimensional changes upon drying, the thickness of samples of each formulation was measured using a digital caliper both before and after the drying phase. The $\Delta\delta$, as a percentage, was calculated as the relative difference between initial and final thickness values ($n = 5$).

The mechanical performance of gelMA-XG matrices was assessed through uniaxial tensile tests, conducted using a universal testing machine (Instron 3365, USA) equipped with a $\pm$ 10 N load cell. Dog-bone shaped specimens (gauge length: 15 mm; width: 5 mm; thickness at the predrying stage: 5 mm) were stretched at a crosshead speed of 10 mm min^{-1} until rupture. The elastic modulus (E) was determined from the slope of the linear region of the stress–strain curves within the ε interval of 5%–20%.

Pull-out Test: A custom-designed setup was developed to evaluate the interfacial shear strength of the hydrogel matrices in a single pull-out test configuration. The system was engineered to securely anchor the hydrogel-based samples during testing, minimizing artifacts due to material elasticity. Tests were conducted under displacement-controlled conditions using a universal testing machine (Instron 3365, USA) equipped with a $\pm$ 10 N load cell. Optical fiber segments were embedded into rectangular samples of matrices (width: 10 mm, length: 35 mm, thickness: 5 mm) at the mid-thickness for a length of 20 mm, before the UV exposure.[23] After that, sample were UV-cured and dried according to the described protocol. Free fiber ends were pulled out at a constant crosshead speed of 5 mm min^{-1}, and the maximum pull-out force was recorded.[43,44] The interfacial shear strength (τ_{app}) was calculated using the following Equation (3)

$$\tau_{\mathrm{app}} = \frac{F_{\max}}{\pi \mathrm{DL}} \tag{3}$$

where F_{max} is the maximum force required to pull the fiber out of the matrix, D is the fiber diameter, L is the length of the embedded fiber.

Adhesion Test: The adhesion of the matrices was measured through a lap shear test using porcine skin as the substrate. Porcine skin was selected because of its well-established similarity to human skin in terms of dermal thickness, collagen architecture, and mechanical behavior, making it a standard biomimetic model for adhesion tests such as lap shear, which cannot be performed directly on human tissue.[39,45–47] Prior to testing, the porcine skin was defatted using a knife to mechanically remove the adipose layer, rinsed thoroughly with distilled water and ethanol, and the epidermis was cleaned with isopropanol (IPA) to eliminate surface residues.[47] Rectangular shapes (70 × 25 mm) were cut and used as substrates. For each formulation, rectangular matrices (10 × 25 × 5 mm, predrying thickness) were prepared and applied to the overlap region between two skin substrates, resulting in a bonded area of the same dimensions. To ensure proper contact, a weight of 500 g was applied and held in place for 5 min. All samples were then tested using a universal testing machine (Instron 3365, USA) equipped with a ± 10 N load cell, at a rate of 5 mm min^{-1} and RT, until matrix-pigskin detachment occurred. The adhesion strength was calculated as the maximum load divided by the initial bonded area.

To further investigate the adhesive properties of the gelMA-XG_{15} matrix on human skin and to assess sensor reusability, a 90° peel test was performed.[19] A rectangular matrix (70 × 15 × 1 mm) was mounted onto a plastic film of the same shape to prevent the stretching of the material during the test. The sample was then gripped by one end to the ±10 N load cell of a universal testing machine (Instron 3365, USA) and subjected to 30 consecutive peel cycles (i.e., attach-peel) on the forearm skin of a healthy volunteer at a peeling rate of 15 mm s^{-1}. The adhesion force of each cycle was determined as the maximum load recorded.

Moreover, several substrates (i.e., aluminum foil, glass, paper, plastic, wood, and cork) were chosen to assess gelMA-XG_{15} matrix adhesion on different materials. For this test, targets with a weight ranging from 3 to 5 g were used.

Fabrication of the FBG-Based Adhesive Wearable Sensor: For the adhesive sensor fabrication, an FBG (AtGrating Technologies, China) with a nominal λ_B of 1541 nm, acrylate recoating, grating length of 10 mm, and a reflectivity of 94%, was employed. The FBG was positioned in the groove of a rectangular mold (50 mm of length, 20 mm of width, 5 mm of thickness), with the sensing segment centered within the mold cavity. The fiber was pretensioned by anchoring both ends to a planar support, ensuring longitudinal alignment. The matrix embedding the fiber was then realized according to the protocol described. Briefly, the gelMA-$XG_{15\%}$ hydrogel solution, preheated to 37 °C, was cast into the mold, and the whole assembly was exposed to UV irradiation at 365 nm for 5 min. After polymerization, the wet sensor was demolded, and placed in a thermostatic oven (G-Therm, AG-System BASIC, Fratelli Galli, Italy) at 37 °C for 24 h for a controlled dehydration and structural stabilization of the fiber–gel assembly.

Metrological Characterization and Assessment: To evaluate the influence of hydrogel encapsulation on the FBG characteristics, the spectral response of the sensor was captured before and after the integration within the matrix, as well as the trend of λ_B was monitored throughout the entire drying process. Measurements were performed using an optical interrogator (si255, Hyperion Platform, LUNA Inc., USA) controlled via ENLIGHT software, with a sampling frequency of 5 Hz for λ_B tracking and 100 Hz for spectra acquisition.

Moreover, sensitivity to both ε (S_ε) and T (S_T) were derived through a metrological assessment. S_ε was determined by clamping the sensor between the grips of a universal tensile testing machine equipped with a ± 500 N load cell (Instron 3365, USA) and applying uniaxial ε from 0% to 1% of the initial gauge length (l_0), at a crosshead speed of 1 mm min^{-1} to simulate quasistatic conditions and RT. Data from both the tensile testing machine and the optical interrogator were recorded at 100 Hz. Ten tensile tests were conducted and the calibration curve ($\Delta\lambda_B$ vs. ε) was computed by averaging the sensor responses and computing the curve that well-fits the experimental data. The expanded uncertainty on S_ε was estimated using a t-Student distribution with 9 degrees of freedom and a confidence level of 95%.

S_T was assessed by exposing the sensor to a controlled thermal gradient in a climatic chamber (KBF-S ECO 240, Binder GmbH, Germany). The test compared the response of the embedded FBG with that of a bare FBG ($\lambda_B = 1557$ nm, acrylate recoating, grating length of 10 mm, and reflectivity of 94%; AtGrating Technologies, China) and a thermistor probe data logger (EL-USB-TP-LCD, LASCAR electronics, UK). All sensors were placed in the chamber and exposed to a ΔT of ≈30 °C through a controlled T ramp from 20 °C to 50 °C over 2 h, at constant relative humidity (i.e., 40%). The FBGs output data were recorded at 5 Hz, while the datalogger acquired at a frequency of 1 Hz. The S_ε and S_T values were calculated as the slope of the best-fitting line relating $\Delta\lambda_B$ to ε and ΔT, respectively.

Moreover, cyclic tensile tests were performed at different controlled strain rates corresponding to 12, 24, and 36 cycles per minute. The sensor was fixed between the grips of the universal testing machine (Instron 3365, USA) equipped with a ± 500 N load cell and subjected to sinusoidal displacement in the 0–1% ε range of the sample initial length l_0 (26 mm). Data from the tensile testing machine and optical interrogator were synchronously recorded at a sampling frequency of 100 Hz.

Preliminary on-Skin Test: The gelMA-$XG_{15\%}$-based sensor was directly adhered onto the skin of a volunteer. Chest and neck were selected for cardio-respiratory activity monitoring, while wrist and knee for joint motion tracking. During each trial, the sensor output was recorded by the optical interrogator at a sampling rate of 100 Hz, and real-time changes in the λ_B were monitored by a laptop equipped with the ENLIGHT software. Tests complied with the Declaration of Helsinki and received approval from the Ethics Committee of Università Campus Bio-Medico di Roma (protocol code: 72.25 CET2cbm ATLETIC, date of approval: 27 May 2025). All participants provided informed written consent before the experiments.

Statistical Analysis: Before being analyzed, datasets were visually inspected for potential outliers and checked for consistency; no transformations or normalizations were required. Data values are presented as mean ± standard deviation (SD), calculated on three independent samples or trials ($n = 3$), unless otherwise specified. Statistical significance between experimental groups was assessed using a pairwise two-sided t-test, with a significance threshold of $\alpha = 5\%$. Asterisks indicate statical significance levels, with p-values < 0.05 (*), < 0.01 (**), < 0.001 (***), else "not significant" (ns). All experimental data were analyzed and processed in MATLAB environment (MathWorks, USA).

Acknowledgments

This work has been partially supported by the Italian MUR under PRIN 2022 "WAYBACK" project.

Conflict of Interest

The authors declare no conflict of interest.

Data Availability Statement

The data that support the findings of this study are available from the corresponding author upon reasonable request.

Keywords

adhesive wearable sensors, fiber Bragg gratings, physiological parameters monitoring, self-adhesive hydrogel matrices

Received: August 11, 2025
Revised: September 30, 2025
Published online: November 12, 2025

[1] J. Heikenfeld, A. Jajack, J. Rogers, P. Gutruf, L. Tian, T. Pan, R. Li, M. Khine, J. Kim,J. Wang, J. Kim, *Lab Chip* **2018**, *18*, 217.
[2] T. Q. Trung, N. Lee, *Adv. Mater.* **2016**, *28*, 4338.
[3] Z. Wang, H. Song, L. Chen, W. Li, D. Yang, P. Cheng, H. Duan, *ACS Appl. Electron. Mater.* **2022**, *4*, 5199.
[4] Z. Wu, X. Li, Z. Feng, C. Wan, Y. Li, T. Li, Q. Yang, X. Liu, M. Ren, J. Li, X. Shang, X. Zhang, X. Huang , *Adv. Healthcare Mater.* **2023**, *12*, 2202629.
[5] G. Giovannini, K. Sharma, L. F. Boesel, R. M. Rossi, *Adv. Healthcare Mater.* **2024**, *13*, 2302603.
[6] L. Zhao, Z. Ren, X. Liu, Q. Ling, Z. Li, H. Gu, *ACS Appl. Mater. Interfaces* **2021**, *13*, 11344.
[7] L. Zhao, J. Zhao, F. Zhang, Z. Xu, F. Chen, Y. Shi, C. Hou, Y. Huang, C. Lin, R. Yu, W. Guo, *Adv. Healthcare Mater.* **2021**, *10*, 2002083.
[8] A. G. Leal-Junior, C. A. R. Diaz, L. M. Avellar, M. J. Pontes, C. Marques, A. Frizera, *Sensors* **2019**, *19*, 3156.
[9] D. Lo Presti, C. Massaroni, M. Zaltieri, R. Sabbadini, A. Carnevale, J. Di Tocco, U. G. Longo, M. A. Caponero, R. D'Amato, E. Schena, D. Formica, *IEEE Sens. J.* **2021**, *21*, 14418.
[10] D. Lo Presti, C. Massaroni, C. S. Jorge Leitao, M. De Fàtima Domingues, M. Sypabekova, D. Barrera, I. Floris, L. Massari, C. M. Loddo, S. Sales, I. I. Iordachita, D. Tosi, E. Schena, *IEEE Access* **2020**, *8*, 156863.
[11] M. Pulcinelli, I. Condò, V. Lavorgna, C. Massaroni, E. Schena, D. Lo Presti, *APL Photonics* **2025**, *10*, 3.
[12] R. Singh, W. Zhang, X. Liu, B. Zhang, S. Kumar, *Opt. Laser Technol.* **2024**, *171*, 110357.
[13] L. Shen, Z. Wang, K. Xiao, C. Teng, S. Kumar, X. Li, R. Min, *IEEE J. Sel. Top. Quantum Electron.* **2024**, *30*, 1.
[14] D. Lo Presti, F. Santucci, C. Massaroni, D. Formica, R. Setola, E. Schena, *Sci. Rep.* **2021**, *11*, 21162.
[15] D. Lo Presti, C. Massaroni, J. D'Abbraccio, L. Massari, M. Caponero, U. G. Longo, D. Formica, C. M. Oddo, E. Schena, *IEEE Sens. J.* **2019**, *19*, 7391.
[16] L. Li, R. He, M. S. Soares, S. Savovic, X. Hu, C. Marques, R. Min, X. Li, *IEEE Sens. J.* **2021**, *21*, 26793.
[17] S. Wang, Y. Fang, H. He, L. Zhang, C. Li, J. Ouyang, *Adv. Funct. Mater.* **2021**, *31*, 2007495.
[18] H. Qu, W. Liang, X. Cheng, H.-Y. Tam, R. Min, P.-C. Li,X. Hu, *IEEE Sens. J.* **2025**, *25*, 4612.
[19] S. H. Jeong, S. Zhang, K. Hjort, J. Hilborn, Z. Wu, *Adv. Mater.* **2016**, *28*, 5830.
[20] F. Han, T. Wang, G. Liu, H. Liu, X. Xie, Z. Wei, J. Li, C. Jiang, Y. He, F. Xu, *Adv. Mater.* **2022**, *34*, 2109055.
[21] X. Liu, H. Yu, L. Wang, Z. Huang, F. Haq, L. Teng, M. Jin, B. Ding, *Adv. Mater. Interfaces* **2022**, *9*, 2101038.
[22] M. Namkoong, H. Guo, M. S. Rahman, D. Wang, C. J. Pfeil, S. Hager, L. Tian, *npj Flexible Electron.* **2022**, *6*, 41.
[23] I. Condò, B. Pizziconi, S. Cimini, M. Trombetta, L. De Gara, E. Schena, S. M. Giannitelli, D. Lo Presti, *IEEE Sens. J.* **2025**, *25*, 2705.
[24] M. Torre, S. M. Giannitelli, E. Mauri, M. Gori, A. Bucciarelli, P. Mozetic, G. Gigli, M. Trombetta, A. Rainer, *Bioprinting* **2023**, *30*, e00262.
[25] N. F. Virzì, P. Diaz-Rodriguez, A. Concheiro, V. Pittalà, C. Alvarez-Lorenzo, *Carbohydr. Polym. Technol. Appl.* **2024**, *7*, 100523.
[26] Z. Yang, X. Ren, Y. Liu, *Mater. Sci. Eng.: C* **2021**, *131*, 112493.
[27] B. Piola, M. Sabbatini, S. Gino, M. Invernizzi, F. Renò, *Int. J. Mol. Sci.* **2022**, *23*, 539.
[28] M. Zhang, J. Ren, R. Li, W. Zhang, Y. Li, W. Yang, *Int. J. Biol. Macromol.* **2024**, *261*, 129718.
[29] D. F. S. Petri, *J. Appl. Polym. Sci.* **2015**, *132*, 23.
[30] C. Pagano, D. Puglia, F. Luzi, A. Di Michele, S. Scuota, S. Primavilla, M. R. Ceccarini, T. Beccari, C. A. V. Iborra, D. Ramella, M. Ricci, L. Perioli, *Pharmaceutics* **2021**, *13*, 1.
[31] M. Mohsin, A. Hossin, Y. Haik, *J. Appl. Polym. Sci.* **2011**, *122*, 3102.
[32] H. Zhang, M. W. Grinstaff, *Macromol. Rapid Commun.* **2014**, *35*, 1906.
[33] H. Li, J. Li, J. Xu, L. Li, Y. Wang, C. Liu, J. Zhou, *Skin Res. Technol.* **2023**, *29*, e13327.
[34] N. Atrux-Tallau, C. Romagny, K. Padois, A. Denis, M. Haftek, F. Falson, F. Pirot, H.I. Maibach, *Arch. Dermatol. Res.* **2010**, *302*, 435.
[35] M. Elsherif, A. E. Salih, M. G. Muñoz, F. Alam, B. AlQattan, D. S. Antonysamy, M. F. Zaki, A. K. Yetisen, S. Park, T. D. Wilkinson, H. Butt, *Adv. Photonics Res.* **2022**, *3*, 2100371.
[36] A. Othonos, *Rev. Sci. Instrum.* **1997**, *68*, 4309.
[37] T. Erdogan, *J. Lightwave Technol.* **1997**, *15*, 1277.
[38] F. Han, X. Xie, T. Wang, C. Cao, J. Li, T. Sun, H. Liu, S. Geng, Z. Wei, J. Li, F. Xu, *Adv. Healthcare Mater.* **2023**, *12*, 2201730.
[39] A. Sigen, Q. Xu, M. Johnson, J. Creagh-Flynn, M. Venet, D. Zhou, I. Lara-Sàez, H. Tai, W. Wang, *Appl. Mater. Today* **2021**, *22*, 100967.
[40] D. Lo Presti, L. Zoboli, C. Massaroni, J. Nedoma, A. Gizzi, E. Schena, *Measurement* **2025**, *253*, 117458.
[41] D. Lo Presti, D. Bianchi, C. Massaroni, A. Gizzi, E. Schena, *Biosensors* **2022**, *12*, 363.
[42] M. Costantini, S. Testa, E. Fornetti, A. Barbetta, M. Trombetta, S. M. Cannata, C. Gargioli, A. Rainer, *Front. Bioeng. Biotechnol.* **2017**, *5*, 22.
[43] J. L. Holloway, A. M. Lowman, M. R. VanLandingham, G. R. Palmese, *Acta Biomater.* **2014**, *10*, 3581.
[44] J. Beter, B. Schrittesser, B. Maroh, E. Sarlin, P. F. Fuchs, G. Pinter, *Polymers* **2020**, *12*, 472.
[45] A. Summerfield, F. Meurens, M. E. Ricklin, *Mol. Immunol.* **2015**, *66*, 14.
[46] C. Uhm, H. Jeong, S. H. Lee, J. S. Hwang, K.-M. Lim, K. T. Nam, *Toxicol. Res.* **2023**, *39*, 477.
[47] H. Zheng, N. Lin, Y. He, B. Zuo, *ACS Appl. Mater. Interfaces* **2021**, *13*, 40013.